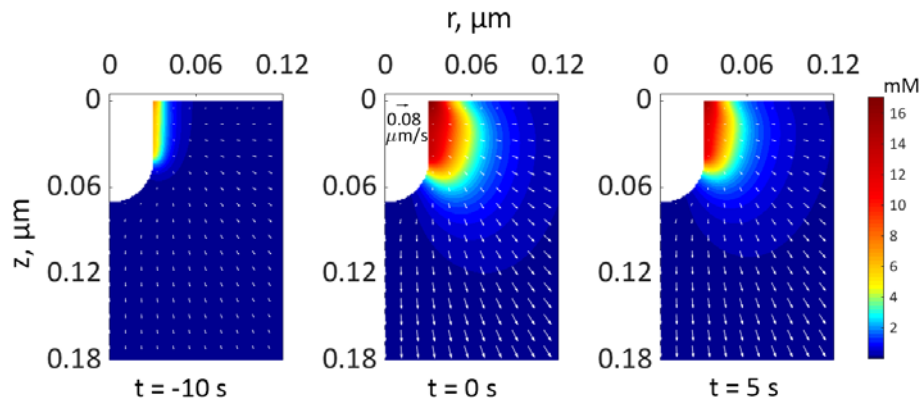# Supplemental Materials
Molecular Biology of the Cell

Nickaeen et al.

Supplemental figures

Figure S1. Simulation of a single ring model of actin patch assembly around a tubule with fixed geometry. Actin densities (color) and velocities (arrows, scale bar in upper-left corner of snapshot in the middle corresponds to 0.08 μm/s) are shown for *r-z* sections of 3D geometry and selected time points. Two rings of nucleation-promoting factors, not shown explicitly, were positioned next to each other at the base of the invagination adjacent to the horizontal portion of the plasma membrane.
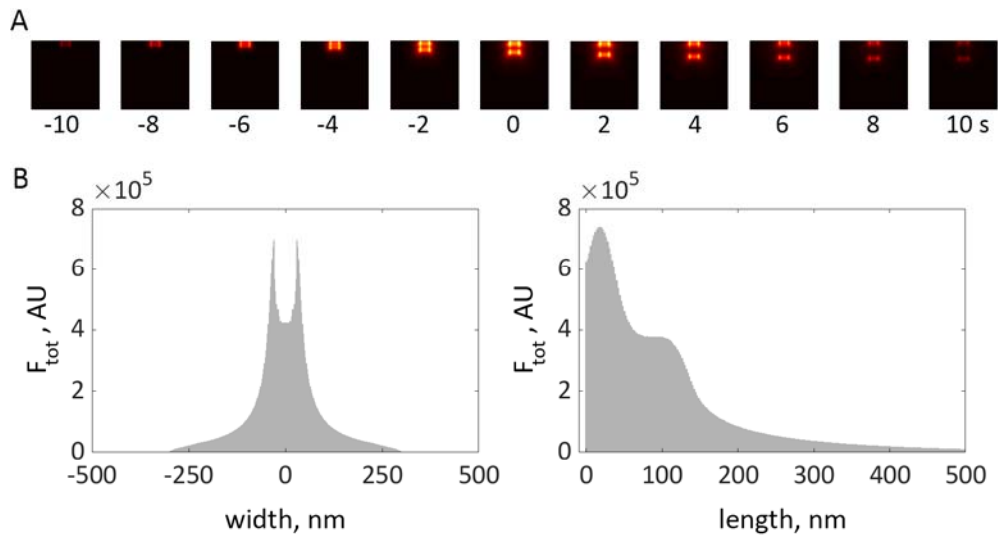
Figure S2. Results of simulating an elongating tubule with two zones of NPFs and a time-dependent force threshold, without applying a median filter. (A) Heatmaps of actin density (see Fig. 7C of main text) are projected on plane for selected time points. (B) Width and length distribution of actin density obtained by integrating the results of panel (A) over time. The central trough in the width distribution reflects the space inside the invagination that is void of actin. No such troughs were observed experimentally, likely because the spatial resolution was comparable to the invagination width.

Supplemental text

1. Model solutions with varying κ_{active} and κ_{visc}

As explained in the main text, solutions of the model are controlled by the ratio $\kappa_{\mathrm{active}}/\kappa_{\mathrm{visc}}$, rather than separately by κ_{active} and κ_{visc}, and the force exerted on the invagination is proportional to κ_{visc}. We confirmed these assertions computationally by solving the model with constant $\kappa_{\mathrm{active}}/\kappa_{\mathrm{visc}}$ over a range of κ_{visc}. Table S1 includes the time-dependent numbers of polymerized subunits in a patch, $n(t)$, and a maximum force $f_{z,\max}$ exerted on a tubule at $t = 0$ s, obtained for varying κ_{visc} and a fixed $\kappa_{\mathrm{active}}/\kappa_{\mathrm{visc}} = 0.94\, n_A^{-1}\ \mathrm{s^{-1} mM^{-1}}$.

Table S1. Number of patch subunits and maximum pulling force for varying κ_{visc} at fixed $\dfrac{\kappa_{\mathrm{active}}}{\kappa_{\mathrm{visc}}}$

κ_{visc}, n_A^{-1} Pa·s/µM	$n(t)$			$f_{z,\max}$, pN
	$t = -10$s	$t = -5$ s	$t = 0$ s	$t = 0$ s
0.94	391.946	2327.21	5231.93	2538.30
0.752	391.947	2327.22	5231.94	2030.70
0.47	391.943	2327.20	5231.93	1269.16

Table S1 indicates, within numerical error, a linear dependence of $f_{z,\max}$ on κ_{visc}, whereas the values of $n(t)$, controlled by $\kappa_{\mathrm{active}}/\kappa_{\mathrm{visc}}$ are essentially independent of κ_{visc} for all selected time points.

2. Modeling the time-dependent force due to turgor pressure

The distribution of forces orthogonal to an invagination (Fig. 6A) suggests that they squeeze the tubule near the plasma membrane and stretch it in the middle. If the tubule were not infinitely rigid, these forces would likely distort the invagination into flask or 'head-and-neck' shape (Fig. 6B), similar to those observed in electron micrographs of budding yeast actin patches (Kukulski et al., 2012). Because turgor pressure is isotropic, the net resistance force f_c it would produce for the flask shape is proportional to the cross-sectional area of the opening of the invagination delineated in Fig. 6B by dashed lines. Indeed, the net force exerted by turgor pressure in the upward direction of the tubule's axis (Fig. 6A) is $\propto \iint \cos\theta\, ds$, where θ ($\theta \in [0,\pi]$) is the angle that the outward, with respect to the cytoplasm, normal vector makes with the upward direction of the axis, ds is the area of an infinitesimal surface element, and the integral is taken over the surface of the invagination. Because $\cos\theta\, ds$ is the signed area of the projection of the surface element on the plane perpendicular to the axis, $\iint \cos\theta\, ds = A_+ - A_-$, where A_+ is the area of the projection of surface points with $\theta \leq \pi/2$, and A_- is the area of the projection of the remaining part of the surface consisting of points with $\theta > \pi/2$. The difference $A_+ - A_-$ is equal

to the cross-sectional area of the opening delineated by the dashed lines in Fig. 6B: $A_+ - A_- = \pi r^2$, where r is the radius of the opening. Thus, f_c decreases as r^2.

We further assume that the radius of the opening, initially equal to the radius of the tubule R, decreases linearly with the normal force $f_n(t)$ (Fig 6C), starting with some threshold value $f_{n,0}$. This yields:

$$r(t) = \begin{cases} R, & \text{for } f_n(t) < f_{n,0} \\ R - k(f_n(t) - f_{n,0}), & \text{for } f_n(t) \geq f_{n,0} \end{cases},$$

where the proportionality coefficient k is chosen so that $r = 0$ for $f_n(t) = f_{n,\max}$, i.e. $k = R/(f_{n,\max} - f_{n,0})$. Then the time-dependent threshold $f_c(t)$, satisfying $f_c(t)/f_{c,\max} = r^2(t)/R^2$, is:

$$f_c(t) = f_{c,\max} \times \begin{cases} 1, & \text{for } f_n(t) < f_{n,0} \\ [(f_{n,\max} - f_n(t))/(f_{n,\max} - f_{n,0})]^2, & \text{for } f_n(t) \geq f_{n,0} \end{cases}.$$

This function is fairly accurately approximated by $f_{c,\max}(1 + \exp((t - t_0)/\tau))^{-1}$, which facilitates incorpotation of the numerically defined $f_n(t)$ in the model. Parameter τ largely reflects the time window of the increase of $f_n(t)$, and t_0 is the timing of the increase of $f_c(t)$, which in part depends on $f_{n,0}$. Varying $f_{n,0}$ causes only marginal changes in simulation outputs. The dashed curve in Fig 7A, obtained with $t_0 = 13$ s and $\tau = 0.66$ s, approximates $f_c(t)$ with $f_{c,\max} = 2538$ pN and $f_{n,0} = 120$ pN.

*3. Actin density and forces at a tip of a tubule.*

Our model yields lower actin filament densities surrounding the tips of the invagination than along the sides, see Figs. 4, 7C, and S1. In Fig. S3A below, we used the results of the simulation of an elongating invagination described in Figs. 4 and 7C to plot the actin density at the surface of the tip as a function of the angle defined in panel B. On the millimolar scale, the actin density is distinctly nonzero only for angles that are greater than 30 degrees.
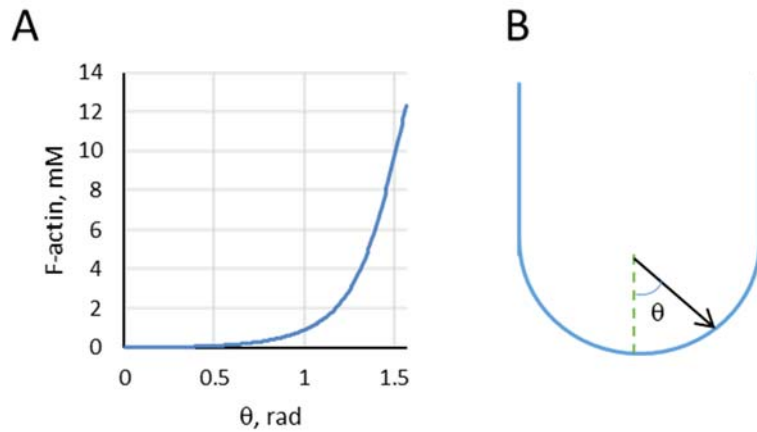
Figure S3. Actin filament density surrounding the tip of invagination. Results for actin density from the simulation of an elongating tubule, as shown in Fig 4, are used to plot the actin density at the surface of the tip (A) as a function of the angle defined in panel (B).

Our simulation results also indicate that the force exerted on the tip by the actin flow, while making up a sizable portion of the net force (for the static geometry, e.g., it is ~ 800 pN, or about a third of the net force), is mostly applied near the junction of the tip with the cylindrical portion of the invagination, so the tip of the invagination lacks the support of actin. Our working assumption is that the tips are sufficiently stiff to resist being crushed in by the turgor pressure. Measurements of rigidity of clathrin-coated vesicles (CCVs) by Jin et al. (2006) support this assumption. According to Fig. 2C in their paper, the force $f = 280$ pN applied to a CCV of radius $R = 50$ nm diminishes the vesicle height by $\Delta H = 45$ nm. The contact area can be approximated as $\pi r^2 = \pi \Delta H (2R - \Delta H / 2)/2$, so that the critical stress is $f /(\pi r^2) \approx 0.5$ atm. The tips of invaginations generally have smaller sizes than CCVs and thus are more rigid, as the rigidity of plates is inversely proportional to the fourth power of their size (Landau and Lifshitz, 1989). Therefore, to endure stresses comparable to turgor pressure of $7 - 9$ atm, the tip radii must be in the $24 - 26$ nm range. These are reasonable estimates of the "mean" radius of the tip, which is midway between the outer and inner radii, i.e. it is the outer radius minus half width of the clathrin coat of the tip.

Due to the low simulated actin density surrounding the tip and the absence of actin in the lumen of the invagination, 'top views' of our simulated actin distributions have deep minima at the center (Fig. S4 A below, where the x- and y- coordinates are shown in nanometers). Such minima are absent from the superresolution data (Mund et al., 2018), which is largely explained
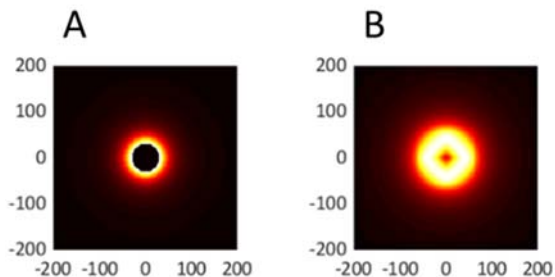
Figure S4. 'Top view' of the simulated actin distribution from Fig. 4: (A) unfiltered simulation results; (B) results of convolving the simulation results in panel (A) with a 30-nm point-spread function.

by the fact that the resolution limit of the single-molecule localization microscopy is ~ 30 nm, which is comparable to the radii of the tubules and to a length scale of actin heterogeneities within a patch. Thus, even super-resolution data would blur the details with sizes below 30 nm. (It is instructive to compare the results of the simulation of an elongating tubule before (Fig. S2) and after applying a filter mimicking the 35-nm resolution of super-resolution microscopy (Fig. 8 of the main text)). Incidentally, the simulation results of Mund et al. also have central minima, though less pronounced (their Fig. S7 D). The quantitative differences of the two models are likely due to different kinetic descriptions of actin nucleation and assembly. The detailed kinetic description employed in our model results in non-uniform distributions of actin with pronounced density peaks in the vicinity of NPFs locations. The Mund et al. actin distribution is much more uniform, because the distribution of active Arp2/3 complex in their model is only weakly correlated with the positions of NPFs (i.e. the distribution of Arp2/3 complex is pretty much uniform throughout the patch, see their Fig. S7 A) and severing by cofilin is ignored.

In both models, the central minima largely disappear upon filtering, see Fig. S4 B above and Figure S7 E in (Mund et al., 2018). The remaining dip in Fig. S4 B may be due to underestimation of the simulated actin densities and/or variations of geometry and sizes of real patches.

4. Methods

M.1 Governing Equations

M1.1 Computational Domain
Based on the assumptions described in *Model*, the computational domain depicted in Figure 1 of the main text remains axisymmetric throughout the elongation process. Because the localization of membrane-bound species and the corresponding fluxes are also axisymmetric, solutions of the model will have the same symmetry. Therefore, the problem reduces to solving an equivalent 2D model in cylindrical coordinates $x = (r, z)$ in the domain Ω shown in Figure M1, where Γ_i ($i =$

1, ..., 5) are the corresponding boundaries. Note that the full 3D geometry is restored by revolving Ω around the axis of symmetry $r = 0$ (red dash-dotted line in Figure M1).
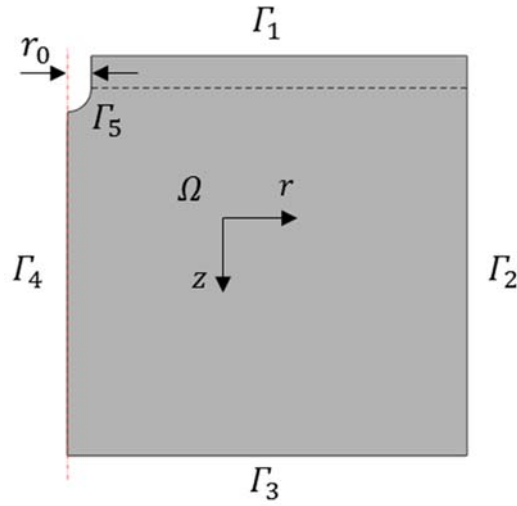

Figure M1. Equivalent 2D axisymmetric computational domain (Ω) and boundaries ($\Gamma_1, \Gamma_2, \Gamma_3, \Gamma_4, \Gamma_5$).

The domain extensions (0.5 µm in each coordinate direction) were chosen to be sufficiently large to ensure that numerical solutions are essentially independent from boundary conditions at Γ_2 and Γ_3 (see the following subsections). The cylindrical and hemispherical parts of the invagination degenerate in the 2D model into a line and a quarter of a circle, respectively. The initial length of the cylindrical part is 40 nm, as it accommodates two rings of nucleation promoting factors (NPFs), each being 20 nm wide (Arasada and Pollard, 2011). The radius of the endocytic invagination is $r_0 = 30$ nm.

M1.2 Transport and Reaction Equations
Spatiotemporal dynamics of proteins involved in patch assembly are governed by conservation of mass, which in our model has the following form,

$$\partial_t [X] = -\nabla \cdot ([X]v) + R_X \qquad \text{in } \Omega \qquad \text{(M1)}$$

for all cytoplasmic species, except ActiveArp (the equation for ActiveArp is discussed below). In Eq (M1), $[X]$ is the concentration of protein X in µM, R_X is the sum of rates of all reactions affecting X, v is actin velocity, and Ω is the computational domain. In what follows, the density of actin network is defined as $\rho = n_A \sum_X [X]$, where the sum is taken over all cytosolic species, except for FArp and ActiveArp, and $n_A = 602$ µm^{-3}/µM.

Functional forms of R_X and parameters are from (Berro et al., 2010), with modifications reflecting the effects of mechanical forces and high local filament densities on polymerization kinetics. In locations where the filament network is dense, molecular diffusion slows down (Novak et al., 2009), which affects reaction rates (Schmit et al., 2009). Because the effective diffusion coefficient of molecules in spaces filled with the filaments reduces by the factor

$(1-\rho/\rho_{max})^{1/2}$ (Novak et al., 2011), we modify by this factor the on- and off- rate constants of polymerization, capping, cofilin binding, and cofilin-dependent severing. This ensures that the abovementioned processes slow down as ρ approaches $\rho_{max} = (4\pi\delta^3/3)^{-1}$, where $\delta = 2.7$ nm is the subunit radius, and, therefore, ρ never exceeds $\rho_{max} = 20.15$ mM. Note that the factor $(1-\rho/\rho_{max})^{1/2}$ is significantly different from unity only where ρ approaches ρ_{max}, so in most locations the rate constants are essentially unchanged. We also take into account that the filaments that generate active stress polymerize under load. The fraction of such filaments is estimated as follows. Assuming that one of the two filament ends is immobilized at the membrane or a branching point, the probability of the filament growing under load is equivalent to that of its other end pushing against the network, which is $p(\mathbf{x},t) = \rho(\mathbf{x},t)/\rho_{max}$. Thus, the affected rates need to be multiplied by $(1- p(\mathbf{x},t)) + p(\mathbf{x},t)\exp(-\sigma_a \delta^3/(k_B T))$. For simplicity, we ignore the contributions of such filaments to actin density altogether, dropping the second term and modifying the rates of polymerization and capping by an additional factor $1- \rho(\mathbf{x},t)/\rho_{max}$.

The equations describing spatiotemporal dynamics of each species are listed below:

$$\partial_t[\text{FArp}] = -\nabla \cdot (\mathrm{v}[\text{FArp}]) + k^+_{\text{Polymerisation}}\, G_0[\text{ActiveArp}] - k_{\text{Chop}}[\text{FCOF}][\text{FArp}] \quad \text{(M2.1)}$$

$$\partial_t[\text{BEa}] = -\nabla \cdot (\mathrm{v}[\text{BEa}]) + k^+_{\text{Polymerisation}}\, G_0[\text{ActiveArp}] + k^-_{\text{Cap}}\,[\text{BEc}]$$
$$-(k^+_{\text{Cap}}C_0 + k_{\text{Chop}}[\text{FCOF}])[\text{BEa}] \quad \text{(M2.2)}$$

$$\partial_t[\text{BEc}] = -\nabla \cdot (\mathrm{v}[\text{BEc}]) + k^+_{\text{Cap}}\, C_0[\text{BEa}]$$
$$- (k^-_{\text{Cap}} + k_{\text{Chop}}[\text{FCOF}] + k^-_{\text{Depolymerization}}\,[\text{PE}]/[\text{Ftot}])[\text{BEc}] \quad \text{(M2.3)}$$

$$\partial_t[\text{PE}] = -\nabla \cdot (\mathrm{v}[\text{PE}]) - (k_{\text{Chop}}[\text{FCOF}] + k^-_{\text{Depolymerization}}\,[\text{BEc}]/[\text{Ftot}])[\text{PE}] \quad \text{(M2.4)}$$

$$\partial_t[\text{FATP}] = -\nabla \cdot (\mathrm{v}[\text{FATP}]) + k^+_{\text{Polymerisation}}\, G_0[\text{BEa}]$$
$$- (k_{\text{Hydrolysis}} + k_{\text{Chop}}[\text{FCOF}] + k^-_{\text{Depolymerization}}\,[\text{PE}]/[\text{Ftot}])[\text{FATP}] \quad \text{(M2.5)}$$

$$\partial_t[\text{FADP}] = -\nabla \cdot (\mathrm{v}[\text{FADP}]) + k_{\text{Hydrolysis}}[\text{FATP}] + k^-_{\text{COFBinding}}\,[\text{FCOF}]$$
$$- (k^+_{\text{COFBinding}}\text{COF}_0 + k_{\text{Chop}}[\text{FCOF}] + k^-_{\text{Depolymerization}}\,[\text{PE}]/[\text{Ftot}])[\text{FADP}] \quad \text{(M2.6)}$$

$$\partial_t[\text{FCOF}] = -\nabla \cdot (\mathrm{v}[\text{FCOF}]) + k^+_{\text{COFBinding}}\, \text{COF}_0[\text{FADP}]$$
$$- (k^-_{\text{COFBinding}} + k_{\text{Chop}}[\text{FCOF}] + k^-_{\text{Depolymerization}}\,[\text{PE}]/[\text{Ftot}])[\text{FCOF}] \quad \text{(M2.7)}$$

In Equations (M2.1) – (M2.7), Ftot = [FADP] + [FATP] + [FCOF] + [PE] + [BEa] + [BEc], and subscript $'0'$ denotes a constant. Values of reaction rate constants and constant concentrations are taken from Table 1 and Table 2 of (Berro et al., 2010). Equations (M2.1) – (M2.7) are subject to zero-flux boundary conditions at the membrane, $\Gamma_{\text{mem}} = \Gamma_1 \cup \Gamma_5$, as well as at the boundary passing along the axis of symmetry Γ_4 in Figure M1. Outflow boundary conditions were enforced at Γ_2 and Γ_3. Note that for solving equations (M2.1) – (M2.7), which are of the hyperbolic type,

boundary conditions need not be specified on all Γ_i (Ferziger and Perić, 2002). However, for technical reasons discussed in subsection *Finite Element Implementation of the Model*, a diffusion term with a very small diffusion coefficient was added to all equations. The resulting parabolic equations require boundary conditions on all boundaries of the domain.

We now describe the equation for ActiveArp. Active Arp2/3 complexes appear in the cytoplasm due to the flux of FArpTernCompl that only exists at the NPF rings (Figure 1 of the main text). The corresponding flux density is $k^+_{\text{ArpActivation}}[\text{FArpTernCompl}]/n_A$, where $[\text{FArpTernCompl}]$ is in molecules/μm². Because the detachment of FArpTernCompl from the membrane involves diffusion, a consistent description of $[\text{ActiveArp}]$ near the rings should include a diffusion term.

The transport terms for all other variables are purely advective, see Eqs (M2.1-M2.7) because our continuous deterministic model does not resolve small distances and ignores fluctuations of the filaments. But since the actin velocities of actin filaments at the membrane are equal to the velocity of the membrane in the continuous approximation, see Eq (M4.2) below, diffusion of the filaments cannot be ignored for ActiveArp near the rings, where it enters the cytoplasm, since otherwise its concentration becomes infinite at those locations.

Therefore, the dynamics of $[\text{ActiveArp}]$ are described by a diffusion-advection-reaction equation,

$$\partial_t[\text{ActiveArp}] = \nabla \cdot (D(x)\nabla([\text{ActiveArp}]) - v[\text{ActiveArp}]) + k^+_{\text{Polymerisation}} G_0[\text{ActiveArp}]$$

$$(\text{M2.8})$$

and a corresponding boundary condition,

$$(D(x)\nabla([\text{ActiveArp}]) + k^+_{\text{ArpActivation}}[\text{FArpTernCompl}]/n_A)|_{\gamma_{\text{rings}}} = 0,$$

where γ_{rings} are the fragments of Γ_{mem} occupied by the rings.

Because the effect of diffusion of ActiveArp is important only at the membrane, the diffusion term is restricted to the vicinity of the rings, by using a diffusion coefficient that is non-zero only along the cylindrical part of the tubule (Γ_5 in Figure M1) and decays exponentially in the radial direction,

$$D(x) = D_{\text{AA}} \exp\left(-\frac{|r - r_0|}{\xi}\right).$$

The parameter values used in the solutions were $\xi = 3$ nm and $D_{\text{AA}} = 0.001$ μm²/s. The choice of ξ was based on the mesh sizes used in the computations. This parameter has little effect on the solution, because ActiveArp quickly converts into BEa, for which the velocity boundary condition is not an issue. Changing the diffusion constant D_{AA} by several orders of magnitude did not change the outcome in any significant way. At all other boundaries, the conditions for $[\text{ActiveArp}]$ were the same as for the other cytoplasmic species.

As in (Berro et al., 2010), adapter proteins that recruit and activate NPFs are not included in our model. Instead, a temporal wave of NPFs with a Gaussian shape drives actin assembly near the rings. Therefore, the surface densities of the membrane-bound proteins are governed by ordinary differential equations (ODEs) based on the rates of corresponding biochemical reactions:

$$\frac{d[\text{WGD}]}{dt} = k^+_{\text{WASpGBinding}} G_0 \text{WASp}_0 e^{\frac{(t-\text{TimePeak})^2}{\sigma}}$$
$$+ k^-_{\text{ArpComplexFormation}}[\text{ArpTernaryComplex}]$$
$$- \left(k^-_{\text{WASpGBinding}} + k^+_{\text{ArpComplexFormation}}\text{Arp}_0\right)[\text{WGD}] \qquad (\text{M3.1})$$

$$\frac{d[\text{ArpTernCompl}]}{dt} = k^+_{\text{ArpComplexFormation}}\text{Arp}_0[\text{WGD}]$$
$$- \left(k^-_{\text{ArpComplexFormation}} + k^+_{\text{WASpGBinding}}([\text{FATP}] + [\text{FADP}])\right)[\text{ArpTernCompl}] \quad (\text{M3.2})$$

$$\frac{d[\text{FArpTernCompl}]}{dt} = k^+_{\text{ArpGWBindingF}}([\text{FATP}] + [\text{FADP}])[\text{ArpTernCompl}]$$
$$- k^+_{\text{ArpActivation}}[\text{FArpTernCompl}] \quad (\text{M3.3})$$

The densities of the membrane-bound species are in $\frac{\text{molecules}}{\mu m^2}$. The reaction rates, initial conditions and other constants are taken from Table 1 and Table 2 of (Berro et al., 2010); note that the value

Table S2. Model variables and their governing equations

variable	definition	governing equation
$\mathbf{x}$	spatial location	
t	time	
$\mathbf{v}(\mathbf{x}, t)$	actin velocity field	(1)
$\rho(\mathbf{x}, t)$	actin filament density, $\rho(\mathbf{x}, t) = n_A \sum_X [X](\mathbf{x}, t)$	(2)
$\eta(\rho, L)$	shear viscosity of actin meshwork	Eq (6)
$\sigma_a(\rho)$	active stress	defined in *Model* of main text
u_z	tubule's elongation speed	Eq (5)
f_z	net tangential force exerted on a tubule	Eq (4)
$D(\mathbf{x})$	diffusion coefficient of ActiveArp	Eq (M2.8)
f_c	critical force due to turgor pressure	defined in *Results*
G_{crit}	critical concentration of actin monomers	defined in *Results*
$w(\rho)$	mechanical work per filament	estimated in *Results*
f_{crit}	buckling force threshold of actin filament	defined in Broedersz and MacKintosh, 2014
FArp	Arp2/3 complex in a filament	(M2.1)
BEa	active barbed ends	(M2.2)
BEc	capped barbed ends	(M2.3)
PE	pointed ends	(M2.4)
FATP	newly polymerized ATP-bound subunits	(M2.5)
FADP	subunits aged by ATP hydrolysis and phosphate dissociation	(M2.6)
FCOF	polymerized subunits bound by cofilin	(M2.7)
ActiveArp	activated Arp2/3 complex	(M2.8)
WGD	WASp - G-actin dimers	(M3.1)
ArpTernCompl	Arp2/3 ternary complexes (Arp2/3 bound to WGD)	(M3.2)
FArpTernCompl	activated Arp2/3 ternary complexes (bound to a filament)	(M3.3)

of WASP$_0$ was converted from μM to $\frac{\text{molecules}}{\text{μm}^2}$. Table S2 provides a list of the model variables and their governing equations.

M1.3 Actin Meshwork Mechanics Equations
The actin meshwork is modeled as a compressible visco-active fluid. In a viscosity-dominated environment of the actin patch, forces due to the fluid's inertia and acceleration are neglected, which leads to a quasi-static formulation of the meshwork velocities v

$$\nabla \cdot (2\eta(\rho, L)\nabla^S v) - \nabla\sigma_a(\rho) = 0, \qquad \text{in} \quad \Omega, \qquad \text{(M4.1)}$$

where $\nabla^S v = 1/2(\nabla v + (\nabla v)^T)$ is the symmetrized velocity gradient tensor, $\eta(\rho, L) = \kappa_{\text{visc}}\rho(1/N + \rho\delta^2 L)$ is the dynamic viscosity, and $\sigma_a = \kappa_{\text{active}}\rho^2$ is the active stress. See subsection *Model* for further details regarding the derivation of the functional forms of the viscosity and the active stress.

Equations (M4.1) are elliptic in nature, similar to the Stokes equations of a Newtonian fluid, and hence require boundary conditions on all boundaries of the computational domain. No-slip boundary condition is applied where actin meshwork meets the membrane

$$v = u \quad \text{at} \quad \Gamma_{\text{mem}}, \qquad\qquad \text{(M4.2)}$$

where u is the velocity of the membrane. All other boundaries are subject to zero-stress boundary conditions,

$$\left(2\kappa_{\text{visc}}\rho(1/N + \rho\delta^2 L)\nabla^S v - \kappa_{\text{active}}\rho^2\, \hat{\text{I}}\right).\mathbf{n} = 0 \quad \text{at} \quad \Gamma_2 \cup \Gamma_3, \quad \text{(M4.3)}$$

where $\hat{\text{I}}$ is a unit tensor and n is the outward normal vector to the boundary.

M1.4 Boundary Conditions and Domain Size Effects
The simulations were first run in a domain with smaller extensions in each coordinate direction, 0.3 μm instead of 0.5 μm. To ensure that the boundary conditions applied at Γ_2 and Γ_3 had no effect on the numerical results, we ran simulations with different types of boundary conditions and in larger domains. No significant changes in the solutions were observed. All the numerical results presented in the paper are from the simulations performed in the larger domains, 0.5 μm in each coordinate direction.

M2 Moving Boundaries Formulation

M2.1 Modelling Tubule Movement
Simulations of elongating invaginations involve additional assumptions. In particular, the shape of the invagination is assumed to remain (sphero)cylindrical during the elongation process, so that only the cylindrical part elongates. Furthermore, we assume for simplicity that the invagination is infinitely rigid, so that all material points move with a same instantaneous velocity, which changes

linearly with the net viscous drag exerted by the actin network; the linear dependence on the pushing force is parameterized by a mobility coefficient, see Equation (5) in *Model*.

From fluid mechanics, the viscous forces acting on the tubule are given by the integral of the total stress in the actin meshwork over the surface of the endocytic invagination,

$$f_{\text{viscous}}(t) = \int_{S(t)} (\hat{\sigma}_{\text{viscous}} + \hat{\sigma}_{\text{active}}) \cdot \mathbf{n} \, dS(t), \tag{M5}$$

In Eq (M5), integration is carried over the time-dependent boundary $S(t) = \Gamma_5(t)$ representing the invagination, and $\mathbf{n} = (n_r, n_z)^T$ is the outward unit normal vector to the boundary $\Gamma_5(t)$ (directed from $\Gamma_5(t)$ towards the interior of $\Omega(t)$). The velocity of the tubule at any given time is then obtained by Eq (5) of *Model*. The z-component of the viscous force is the drag force exerted on the invagination, $f_z(t) = f_{\text{viscous}}(t) \cdot n_z$, and the force due to the turgor pressure Π_{turgor}, is $f_c = \pi r_0^2 \Pi_{\text{turgor}}$, where r_0 is the radius of the (sphero)cylindrical invagination (Figure M1); if the invagination is constricted by the surrounding meshwork, r_0 is the radius of the pore between the exterior and the lumen of the invagination.

M2.2 The ALE Framework
The models of elongating invaginations were solved using an Arbitrary Lagrangian-Eulerian (ALE) method. The ALE method is described in numerous publications, see e.g. (Donea et al., 2004). In an ALE simulation, the computational mesh moves with displacements/velocities prescribed at the boundaries of interest (normally loading and interface boundaries). At all other places in the domain, the mesh moves with a smooth arbitrary velocity such that mesh quality is maintained throughout the simulation, while mesh connectivity remains the same. The governing equations formulated in a Eulerian coordinate system should be reformulated based on the ALE framework. Following the notation used by (Formaggia and Nobile, 2004), a fixed reference frame $\tilde{\Omega}$ and a mapping $\mathcal{A}_t : \tilde{\Omega} \rightarrow \Omega(t)$ is defined to provide a one-to-one correspondence $x = \mathcal{A}_t(\tilde{x})$, and $\tilde{x} = \mathcal{A}_t^{-1}(x)$ between the Eulerian coordinates $x = (r, z) \in \Omega(t)$ and ALE coordinates $\tilde{x} = (\tilde{r}, \tilde{z}) \in \tilde{\Omega}$. It is straightforward to show that for any scalar function $f(x, t)$, the Eulerian and ALE time derivatives are related by the chain rule,

$$\left. \frac{\partial f}{\partial t} \right|_{\tilde{x}} = \left. \frac{\partial f}{\partial t} \right|_x + \left. \frac{\partial x}{\partial t} \right|_{\tilde{x}} \cdot \nabla f = \left. \frac{\partial f}{\partial t} \right|_x + \mathbf{v}_m \cdot \nabla f \tag{M6},$$

where $\mathbf{v}_m(x, t) = \left. \frac{\partial x}{\partial t} \right|_{\tilde{x}} (\tilde{x}, t)$ is the local mesh velocity. The mesh velocity can be obtained by solving in the domain a mesh smoothing equation. See *Finite Element Implementation of the Model* for further details.

Since domain $\Omega(t)$ changes with time, it is generally not possible to discretize directly the Eulerian time derivatives in the transport-reaction equations. In fact, if $x \in \Omega(t)$ and $\Delta t > 0$, the condition $x \in \Omega(t + \Delta t)$ may not be always satisfied (San Martín et al. 2009). Therefore, the Eulerian time derivatives $\left. \frac{\partial f}{\partial t} \right|_x$ in the transport-reaction equations are substituted by the right-hand side of equation (M6). This introduces additional advection-like terms to the equations with the advection

velocity being the local mesh velocity v_m. For example, the transport equation (M1) in the equivalent ALE formulation reads as

$$\left.\frac{\partial X}{\partial t}\right|_{\tilde{x}} - v_m \cdot \nabla X = -\nabla \cdot ([X]v) + R_X \qquad \text{in } \Omega(t). \qquad \text{(M7)}$$

It should be noted that all space derivatives in Equation (M7) are taken with respect to the Eulerian coordinates x. This equation is subject to Rankine-Hugoniot boundary condition (zero-flux boundary condition) on the moving boundary $\Gamma_5(t)$. Boundary conditions on all other non-moving boundaries remain unchanged.

The equations for actin meshwork mechanics and their boundary conditions do not change in the ALE framework. This is because these equations are in quasi-static form and there are no history-dependent rates in the definitions of viscous and active stresses (Donea et al., 2004).

ODEs that govern membrane-bound species are not modified as a result of the movement, since these species are treated in the model as non-spatial.

M2.3 Movement of the NPF Ring(s)
According to the two-ring hypothesis (Arasada and Pollard, 2011), two NPF rings drive the actin assembly. One of the rings remains stationary near the horizontal membrane, Γ_1 in Figure M1. The other ring moves with the tubule, keeping its proximity to the tip of the tubule. During the movement the width of the NPF rings and their radius remain constant. Therefore, it suffices to track the z-component of the position of the moving ring z_{ring} described by

$$\frac{dz_{\text{ring}}}{dt} = u_z(t), \qquad \text{(M8)}$$

where $u_z(t)$ is as in Eq (5) of *Model*. The movements of the rings were tracked similarly in the one-ring models described in *Results*.

M3 Finite Element Implementation of the Model
We used a Galerkin finite-element method to solve numerically the governing equations for the transport and reaction of proteins, and the equation for velocities of the actin meshwork. These equations are implemented and solved in COMSOL Multiphysics (COMSOL, 2015) in a 2D axisymmetric domain (Figure M1), as described below.

M3.1 Computational Mesh
A computational mesh used for spatial discretization of the governing equations consisted of 33777 quadrilateral elements (Figure M2(a)). To approximate the velocity gradients near the invagination with more precision, a boundary layer mesh was constructed. These gradients are important for calculating forces exerted on the tubule, and they affect the accuracy of the numerical solution overall. Figure M2(b) is a zoomed-in view of the vicinity of the invagination to show the boundary layer mesh.

The mesh was designed so that as the tubule grew, the elements near the horizontal membrane and in the vicinity of the cylindrical part of the tubule were elongated in the *z* direction. To maintain sufficiently fine elements even after they were stretched as a result of the elongation, a high initial mesh density was used in the vertical direction in these regions. For more details about the design of mesh movements and its implementation see subsection *Mesh Smoothing Equations* below.

Classical mesh refinement was performed for simulations in fixed geometries and for one simulation of an elongating invagination to ensure that numerical results were grid-independent. The original mesh was refined by reducing the linear size of elements by approximately a factor of 2. This yielded 132884 quadrilateral elements, roughly four times the number of elements in the original mesh. The solutions obtained with refined meshes differed from the original mesh by less than 0.3%.

Given the negligible differences, all subsequent moving geometry simulations were performed on the original mesh.
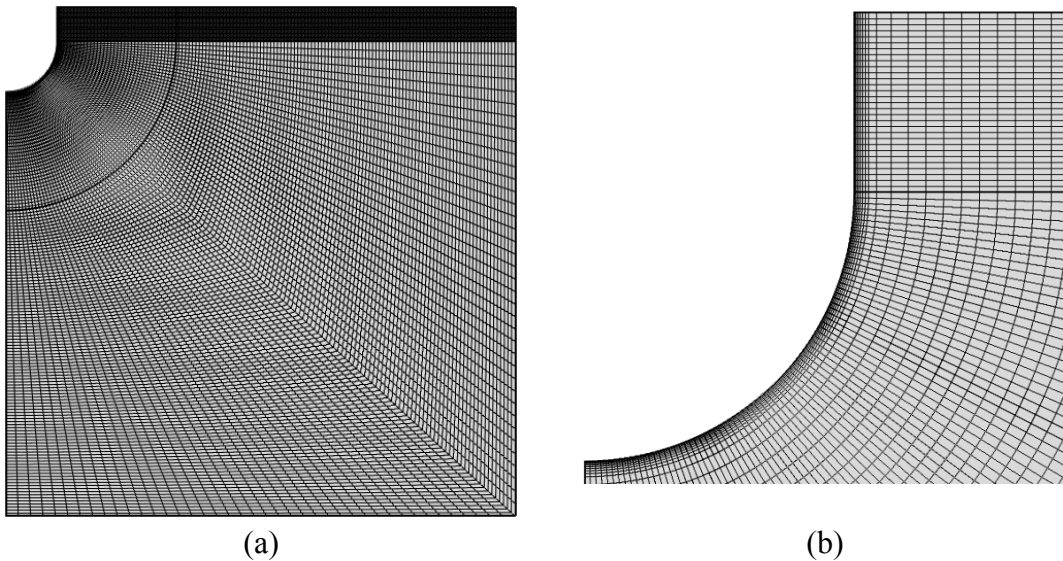

(a)   (b)

Figure M2. The computational mesh(a), and a zoomed-in view near the invagination boundaries (b).

M3.2 Transport Equations of Cytoplasmic Species

Eqs (M2.1-M2.8), governing the spatiotemporal dynamics of cytosolic species, were solved using COMSOL's 'Transport of Diluted Species' module. For simulating moving domains, the module automatically adds to the transport equations advection-like terms of Eq (M7). Linear Lagrange finite elements were used to approximate the concentrations of these species.

Solving Eqs (M2.1-M2.7) with the standard Galerkin finite-element method may result in spurious oscillations (Donea and Huerta, 2003). Treating advection terms with Petrov-Galerkin type methods available in COMSOL can suppress these unphysical oscillations. However, the effectiveness of these methods generally depends on values of auxiliary parameters, and some numerical oscillations may persist. We chose instead adding to the transport equations a diffusion term with a small diffusion coefficient, termed 'technical diffusion' with diffusivity $D_{\text{tech.}}$, and

using standard discretization schemes for all terms. For consistency, $D_{\text{tech.}}$ was added also to $D(x)$ in Eq (M2.8) for [ActiveArp]. In all simulations, we used the value $D_{\text{tech.}} = 1 \times 10^{-5} \mu m^2/s$. Decreasing $D_{\text{tech.}}$ further by an order of magnitude did not produce significant changes in the solution. While spurious oscillations can occur in solving diffusion-advection equations on meshes with high Peclet numbers, no such oscillations were observed after adding technical diffusion for the meshes used in our computations (see subsection M3.1).

M3.3 ODEs for Membrane-bound Species

Eqs (M3.1-M3.3) for membrane-bound species were solved on Γ_5 (Figure M1) with the 'Boundary ODEs and DAEs' module of COMSOL. Positions of the rings of NPFs were accounted for by multiplying the first term in the right-hand side of Eq (M3.1) by a Boolean expression, which was evaluated to one at the locations of the rings and zero elsewhere. As the rings moved, the expression was updated accordingly. Although, membrane-bound species are non-zero only at the locations of the rings, the corresponding ODEs were solved everywhere on Γ_5, allowing for a uniform application of the flux boundary condition for [ActiveArp], although the flux density was non-zero only at γ_{rings}. Constant discontinuous Lagrange finite elements were used for the membrane-bound species.

M3.4 Velocity Equations

Eqs (M4.1) for actin velocities were solved using the 'Weak Form PDE' module of COMSOL, which allows one to implement a method of weighted residuals solving equations in weak forms (Donea and Huerta, 2003). Let $\mathcal{W}$ be the space of weighting (test) functions vanishing on the Dirichlet boundaries Γ_{mem}, and let $w(w_1, w_2, w_3) \in \mathcal{W}$ be the test functions for velocities in the cylindrical coordinates. The weighted residual form of equations in the moving domain $\Omega(t)$ is then written as

$$\int_{\Omega(t)} w \left[\nabla \cdot \left(2\eta(q,L)\nabla^S v - \kappa_{\text{active}}q^2 \hat{I} \right) \right] dx = 0 \qquad \forall w \in \mathcal{W}, \quad \text{(M9)}$$

where q and v are the weak solutions corresponding to the polymerized actin density ρ and actin velocities v. The weak solution v resides in a space of admissible functions satisfying the Dirichlet (no-slip) boundary condition (M4.2). Integrating by parts and applying Green's formula (Donea and Huerta, 2003) then yields

$$\int_{\Omega(t)} \nabla w : \left(2\eta(q,L)\nabla^S v - \kappa_{\text{active}}q^2 \hat{I} \right) dx$$
$$- \int_{\Gamma(t)\backslash\Gamma_{\text{mem}}} w \cdot \left(2\eta(q,L)\nabla^S v - \kappa_{\text{active}}q^2 \hat{I} \right) \cdot n \ ds = 0 \quad \forall w \in \mathcal{W}, \quad \text{(M10)}$$

where ':' denotes the double dot product of two tensors. The integrand in the second integral of equation (M10) is zero on $\Gamma(t)\backslash\Gamma_{\text{mem}}$ due to the zero-stress boundary condition (M4.3), so the final weak form of the velocity equations reads

$$\int_{\Omega(t)} \nabla w : \left(2\eta(q,L)\nabla^S v - \kappa_{\text{active}}q^2 \hat{I} \right) dx = 0 \qquad \forall w \in \mathcal{W}. \quad \text{(M11)}$$

To derive equations for velocity components in weak form for the equivalent two-dimensional axisymmetric coordinate system, one should start with the full differential operators in cylindrical coordinates (r, θ, z), and then remove θ-components and derivatives with respect to θ. In a cylindrical coordinate system with orthonormal basis vectors $\bar{r}, \bar{\theta}, \bar{z}$, the velocity gradient operator and the symmetrized velocity gradient tensor applied to the weak solution $v = (v_1, v_2, v_3)^T$ are defined as follows:

$$\nabla v = \frac{\partial v_1}{\partial r}\bar{r}\,\bar{r} + \frac{\partial v_2}{\partial r}\bar{\theta}\bar{r} + \frac{\partial v_3}{\partial r}\bar{z}\bar{r} + \frac{1}{r}\left(\frac{\partial v_1}{\partial \theta} - v_2\right)\bar{r}\bar{\theta} + \frac{1}{r}\left(v_1 + \frac{\partial v_2}{\partial \theta}\right)\bar{\theta}\bar{\theta} + \frac{1}{r}\frac{\partial v_3}{\partial \theta}\bar{z}\bar{\theta} + \cdots$$
$$\frac{\partial v_1}{\partial z}\bar{r}\bar{z} + \frac{\partial v_2}{\partial z}\bar{\theta}\bar{z} + \frac{\partial v_3}{\partial z}\bar{z}\bar{z}, \qquad\qquad\qquad\qquad\qquad\qquad \text{(M12)}$$

$$\nabla^S v = \frac{1}{2}(\nabla v + (\nabla v)^T) = \frac{\partial v_1}{\partial r}\bar{r}\bar{r} + \frac{1}{2}\left(\frac{\partial v_2}{\partial r} + \frac{1}{r}\left(\frac{\partial v_1}{\partial \theta} - v_2\right)\right)\bar{\theta}\bar{r} + \frac{1}{2}\left(\frac{\partial v_3}{\partial r} + \frac{\partial v_1}{\partial z}\right)\bar{z}\bar{r} + \cdots$$
$$\frac{1}{2}\left(\frac{\partial v_2}{\partial r} + \frac{1}{r}\left(\frac{\partial v_1}{\partial \theta} - v_2\right)\right)\bar{r}\bar{\theta} + \frac{1}{r}\left(v_1 + \frac{\partial v_2}{\partial \theta}\right)\bar{\theta}\bar{\theta} + \frac{1}{2}\left(\frac{1}{r}\frac{\partial v_3}{\partial \theta} + \frac{\partial v_2}{\partial z}\right)\bar{z}\bar{\theta} + \cdots$$
$$\frac{1}{2}\left(\frac{\partial v_3}{\partial r} + \frac{\partial v_1}{\partial z}\right)\bar{r}\bar{z} + \frac{1}{2}\left(\frac{1}{r}\frac{\partial v_3}{\partial \theta} + \frac{\partial v_2}{\partial z}\right)\bar{\theta}\bar{z} + \frac{\partial v_3}{\partial z}\bar{z}\bar{z}. \qquad\qquad \text{(M13)}$$

A unit tensor is defined as $\hat{I} = \bar{r}\,\bar{r} + \bar{\theta}\bar{\theta} + \bar{z}\bar{z}$. Using these definitions, the first term in the integrand of equation (M11), $\nabla w : (2\eta(q, L)\,\nabla^S v)$, is

$$\nabla w : (2\eta(q, L)\,\nabla^S v) = 2\eta(q, L)\left[\frac{\partial w_1}{\partial r}\frac{\partial v_1}{\partial r} + \frac{\partial w_2}{\partial r}\frac{1}{2}\left(\frac{\partial v_2}{\partial r} + \frac{1}{r}\left(\frac{\partial v_1}{\partial \theta} - v_2\right)\right)\right.$$
$$+ \frac{\partial w_3}{\partial r}\frac{1}{2}\left(\frac{\partial v_3}{\partial r} + \frac{\partial v_1}{\partial z}\right) + \frac{1}{r}\left(\frac{\partial w_1}{\partial \theta} - w_2\right)\frac{1}{2}\left(\frac{\partial v_2}{\partial r} + \frac{1}{r}\left(\frac{\partial v_1}{\partial \theta} - v_2\right)\right) + \frac{1}{r}\left(w_1 + \frac{\partial w_2}{\partial \theta}\right)\frac{1}{r}\left(v_1 + \frac{\partial v_2}{\partial \theta}\right)$$
$$\left. + \frac{1}{r}\frac{\partial w_3}{\partial \theta}\frac{1}{2}\left(\frac{1}{r}\frac{\partial v_3}{\partial \theta} + \frac{\partial v_2}{\partial z}\right) + \frac{\partial w_1}{\partial z}\frac{1}{2}\left(\frac{\partial v_3}{\partial r} + \frac{\partial v_1}{\partial z}\right) + \frac{\partial w_2}{\partial z}\frac{1}{2}\left(\frac{1}{r}\frac{\partial v_3}{\partial \theta} + \frac{\partial v_2}{\partial z}\right) + \frac{\partial w_3}{\partial z}\frac{\partial v_3}{\partial z}\right].$$

The simplification due to axial symmetry yields the following weak form of the first term in Eq (M11):

$$\int_{\Omega(t)} 2\pi r\, \nabla w : (2\eta(q, L)\nabla^S v)\, dx$$

$$= \int_{\Omega(t)} 2\pi r\, 2\eta(q, L)\left[\frac{\partial w_1}{\partial r}\frac{\partial v_1}{\partial r} + \frac{1}{2}\frac{\partial w_3}{\partial r}\left(\frac{\partial v_3}{\partial r} + \frac{\partial v_1}{\partial z}\right) + \frac{w_1}{r}\frac{v_1}{r}\right.$$
$$\left. + \frac{1}{2}\frac{\partial w_1}{\partial z}\left(\frac{\partial v_3}{\partial r} + \frac{\partial v_1}{\partial z}\right) + \frac{\partial w_3}{\partial z}\frac{\partial v_3}{\partial z}\right] dx \qquad \text{(M14)}$$

Similarly, the second term of the integrand in Eq (M11) yields

$$-\nabla w : \left(\kappa_{\text{active}}q^2\,\hat{I}\right) = -\kappa_{\text{active}}q^2\left(\frac{\partial w_1}{\partial r} + \frac{1}{r}\left(w_1 + \frac{\partial w_2}{\partial \theta}\right) + \frac{\partial w_3}{\partial z}\right),$$

and upon the reduction due to axial symmetry, the weak form of the second term in Eq (M11) is

$$\int_{\Omega(t)} -2\pi r \, \nabla w : \left(\kappa_{\text{active}} q^2 \, \hat{I} \right) dx = \int_{\Omega(t)} -2\pi r \, \kappa_{\text{active}} q^2 \left(\frac{\partial w_1}{\partial r} + \frac{w_1}{r} + \frac{\partial w_3}{\partial z} \right) dx. \quad \text{(M15)}$$

The factor $2\pi r$ in Eqs (M14-15) is the result of integration over θ.

Eqs (M14) and (M15) were implemented in COMSOL. Linear Lagrange finite elements were used in computing actin velocities.

M3.5 Mesh Smoothing Equations
Solving a moving boundary problem using the ALE method requires computing local mesh velocities v_m. While v_m are not known in advance in the interior of the domain, velocities of points on a moving tubule are computed from Eq (5) of *Model*, while other boundaries of the computational domain are fixed in the course of a simulation. To correctly model the movements of the domain, mesh velocities at the boundaries should coincide with the velocities of the boundary. Then the mesh velocities of the interior points of the domain may be computed, for instance, by employing a harmonic extension of the boundary velocities (Formaggia and Nobile, 2004).

Computing v_m and tracking of mesh movements were done using the 'Moving Mesh' module of COMSOL, which allows one to prescribe mesh displacements x_m and/or mesh velocities at the domain boundaries and at any other interior domain points/edges. Values of v_m in the domain interior were computed using a Laplacian mesh smoother with linear geometric shape functions. Care must be exercised in simulating large elongations, which may result in a highly distorted mesh. The ALE methods become instable on distorted meshes, so that the domain needs to be remeshed to restore the regularity of the elements (San Martín et al., 2009). Remeshing entails interpolation to a new mesh, which introduces additional error. Also, frequent remeshing increases computational costs. To avoid remeshing and the issues associated with it, we defined a virtual edge in the interior of the computational domain, indicated by a dashed line in Figure M1. The tubule velocity computed from Eq (5) in *Model* was then used as the z-component of the mesh velocity for both the virtual edge and the circular part of Γ_5. The r-components of the mesh velocity on these segments were set to zero. The prescribed movement of the virtual edge guides the mesh deformation in the interior of the domain and allows for modeling very large tubule elongations without remeshing. On Γ_2, Γ_4 and the straight part of Γ_5, the r-component of the mesh displacement was set to zero, whereas the vertical components was allowed to vary freely. Displacements of the mesh on the remaining horizontal segments of the domain boundary were set to zero.

M3.6 Equation for Updating NPF Ring Position
Eq (M8), determining the time-dependent z-component of the position of the moving ring, z_{ring}, was solved using COMSOL's 'Point ODEs and DAEs' module for one point on Γ_5. The z_{ring} was initialized to the position of the ring at $t = 0$. Because Eq (M8) was solved in COMSOL within a spatial model, a constant discontinuous Lagrange finite element was used to approximate z_{ring}.

M4 Solvers and Computational Parameters
The coupled nonlinear system of equations describing the cytoplasmic species, Eqs (M2.1- 8), the membrane-bound species, Eqs (M3.1-3), the ring's position Eq (M8), and the actin velocities, Eqs (M14-15), along with the corresponding boundary conditions, were discretized using FEM and solved in a fully coupled manner in COMSOL. Note that even though the force-balance equation does not involve time derivatives, the coupled system constitutes an initial-value problem, so that initial conditions must be specified for all variables (initial values of the actin velocities were set to zero).

The time-dependent system was solved using a backward-differentiation time-stepping method of order 1-2. Relative and absolute tolerances of the time-stepper were set to 1×10^{-5} and 1×10^{-6}, respectively. Other default solver parameters were used without modification. Linearization was performed using Newton's method with a constant damping factor of 1. The system's Jacobian was updated at each nonlinear iteration. The linearized system was solved monolithically using a direct MUMPS solver with default solver parameters. We verified, by solving the problem with varying solver parameters (including the tolerances of the time-stepper), that the solutions did not depend on specific choices of parameters of the solver.

M5 Data Analysis and Display
Presentation and post-processing of numerical results were facilitated by exporting the COMSOL FEM solutions, obtained at the Lagrange points, which were further processed in MATLAB R2017b (The MathWorks, Natick, MA). The 2D snapshots of the solution (see, as an example, Figs. 4 and S1) were obtained by interpolating the FEM solutions onto a uniform 2D grid. A sufficiently large size of the grid allowed for accurately capturing all important features of the FEM solution that were first visualized in COMSOL. The 3D snapshots (see, for instance, Movies S1 and S2) were exported as image files from COMSOL and then replotted in MATLAB.

The actin filament heat maps in Figs. 8 and S2 were produced by first interpolating the FEM solutions for polymerized actin onto a uniform 3D grid defined inside a domain with the horizontal and vertical extensions of $[-0.5, 0.5]$ µm and $[0, 0.5]$ µm, equal to the respective ranges of r and z coordinates of the 2D axisymmetric model. The extension in the depth direction was $[-0.2, 0.2]$ µm, in accordance with the thickness of the imaging plane in epifluorescence microscopy experiments of (Arasada et al., 2018). The interpolated 3D data was then projected on a 2D plane by integrating over the depth direction; the corresponding heat maps are presented in Fig. S2. The projected data were further subjected to a median filter with a half window size of 35 nm; the heat maps for the filtered data are shown in Fig. 8 of the main text.

The histograms in Figs. 8 and S2 were produced as follows. First, the filtered projected (projected only for Fig. S2) data were integrated over time. This yielded a two-dimensional matrix with the elements corresponding to the 2D image of the actin filament density integrated over time. In accordance with the protocol adopted by (Arasada et al., 2018), the width (length) distribution of the actin density was generated by summing up the values of the elements in each column (row) of the matrix. The width of the patch was calculated as the width of the corresponding histogram at half its maximum.

References

Arasada, R., and T.D. Pollard. 2011. Distinct roles for F-BAR proteins Cdc15p and Bzz1p in actin polymerization at sites of endocytosis in fission yeast. *Curr. Biol.* 21:1450-1459

Arasada, R., W.A. Sayyad, J. Berro and T.D. Pollard. 2018. High-speed super resolution imaging of the proteins in fission yeast clathrin-mediated endocytic actin patches. *Mol. Biol. Cell* 29:295-303.

Berro, J., V. Sirotkin, and T.D. Pollard. 2010. Mathematical Modeling of Endocytic Actin Patch Kinetics in Fission Yeast: Disassembly Requires Release of Actin Filament Fragments. *Mol. Biol. Cell.* 21: 2905–2915.

COMSOL Multiphysics. 2015. Version 5.2 [software]. Stockholm, Sweden: COMSOL AB. Available from: www.comsol.com.

Donea, J., and A. Huerta. 2003. *Finite Element Methods for Flow Problems*, John Wiley & Sons.

Donea, J., A. Huerta, J.-Ph. Ponthot, and A. Rodriguez-Ferran. Arbitrary Lagrangian–Eulerian Methods. 2004. In Stein, E., R. de Borst, and T.J.R. Hughes (eds) *Encyclopedia of Computational Mechanics*. Volume 1: *Fundamentals*, John Wiley & Sons.

Ferziger, J. H., and M. Perić. 2002. *Computational Methods for Fluid Dynamics*, Springer.

Formaggia L., and F. Nobile. 2004. Stability analysis of second-order time accurate schemes for ALE–FEM. *Comput. Methods Appl. Mech. Engrg.* 193: 4097–4116.

Jin, A.J., K. Prasad, P.D. Smith, E.M. Lafer, and R. Nossal. 2006. Measuring the Elasticity of Clathrin-Coated Vesicles via Atomic Force Microscopy. *Biophys. J.* 90:3333-3344.

Kukulski, W., M. Schorb, M. Kaksonen, and J. A. Briggs. 2012. Plasma membrane reshaping during endocytosis is revealed by time-resolved electron tomography. *Cell* 150:508-20.

Landau, L. D., and E.M. Lifshitz. 1989. *Theory of Elasticity: Volume 7(Course of Theoretical Physics)*, Pergamon Press.

Mund, M., J. A. van der Beek, J. Deschamps, S. Dmitrieff, P. Hoess, J-L. Monster, A. Picco, F. Nédélec, M. Kaksonen, and J. Ries. 2018. Systematic nanoscale analysis of endocytosis links efficient vesicle formation to patterned actin nucleation. *Cell* 174:884-896.

Novak, I.L., F. Gao, P. Kraikivski, and B.M. Slepchenko. 2011. Diffusion amid random overlapping obstacles: Similarities, invariants, approximations. *J. Chem. Phys.* 134:154104.

Novak, I.L., P. Kraikivski, and B.M. Slepchenko. 2009. Diffusion in cytoplasm: effects of excluded volume due to internal membranes and cytoskeletal structures. *Biophys J.* 97:758-67.

San Martín, J., L. Smarandab, and T. Takahashi. 2009. Convergence of a finite element/ALE method for the Stokes equations in a domain depending on time. *J. Comput. Appl. Math.* 230: 521-545.

Schmit, J. D., E. Kamber, and J. Kondev 2009. Lattice Model of Diffusion-Limited Bimolecular Chemical Reactions in Confined Environments. *Phys. Rev. Lett.* 102: 218308.